

Subvoxel Segmentation and Representation of Brain Cortex Using Fuzzy Clustering and Gradient Vector Diffusion

Ming-Ching Chang
changm@research.ge.com

Xiaodong Tao
taox@research.ge.com

GE Global Research Center, Niskayuna NY USA

ABSTRACT

Segmentation and representation of human brain cortex from Magnetic Resonance (MR) images is an important step for visualization and analysis in many neuro imaging applications. In this paper, we propose an automatic and fast algorithm to segment the brain cortex and to represent it as a geometric surface on which analysis can be carried out. The algorithm works on T1 weighted MR brain images with extracranial tissue removed. A fuzzy clustering algorithm with a parametric bias field model is applied to assign membership values of gray matter (GM), white matter (WM), and cerebrospinal fluid (CSF) to each voxel. The cortical boundaries, namely the WM-GM and GM-CSF boundary surfaces, are extracted as iso-surfaces of functions derived from these membership functions. The central surface (CS), which traces the peak values (or *ridges*) of the GM membership function, is then extracted using *gradient vector diffusion*. Our main contribution is to provide a generic, accurate, fast, yet fully-automatic approach to (i) produce a soft segmentation of the MR brain image with intensity field correction, (ii) extract both the boundary and the center of the cortex in a surface form, where the topology and geometry can be explicitly examined, and (iii) use the extracted surfaces to model the curvy, folding cortical volume, which allows an intuitive measurement of the thickness. As a demonstration, we compute cortical thickness from the surfaces and compare the results with what has been reported in the literature. The entire process from raw MR image to cortical surface reconstruction takes on average between five to ten minutes.

Keywords: cerebral cortex, tissue classification, intensity inhomogeneity, bias field correction, central surface, gradient vector diffusion, anisotropic diffusion, cortical thickness.

1. INTRODUCTION

The segmentation and representation of human brain cortex from Magnetic Resonance (MR) images is a fundamental step in many medical imaging applications, including the visualization and diagnostic analysis in pathology and clinics. Applications relying on using the morphologic contents of the MR images often require classification of the image volume into tissue types, an important problem that has received extensive studies.¹⁻³ Specifically, two major issues arise when performing tissue classification on MR images in practice. First, classifying tissue voxels exclusively into distinct classes is impractical, since artifacts like the *partial volume effect* are omnipresent due to limited image resolution. Therefore, the *soft* segmentation techniques¹ has drawn growing attention, where voxels are labelled into multiple classes with a likelihood of membership value of each class. Secondly, MR images typically contain intensity inhomogeneities arising from the imperfections in acquisition.^{4,5} This artifact causes varying intensities of the same tissue and hinders standard segmentation algorithms such as region growing to work properly. Typical solution is to estimate a smooth *intensity (gain) field* to compensate the inhomogeneities prior to performing tissue classification.^{1,2}

This work is partly supported by the National Alliance for Medical Image Computing, Grant U54 EB005149, and Development and Dissemination of Robust Brain MRI Measurement Tools, Grant R01 EB006733. This work is part of the National Alliance for Medical Image Computing, funded by the National Institutes of Health through the NIH Roadmap for Medical Research, Grant U54 EB005149. Information on the National Centers for Biomedical Computing can be obtained from <http://nihroadmap.nih.gov/bioinformatics>. It is also supported by NIH Grant R01 EB006733, "Development and Dissemination of Robust Brain MRI Measurement Tools".

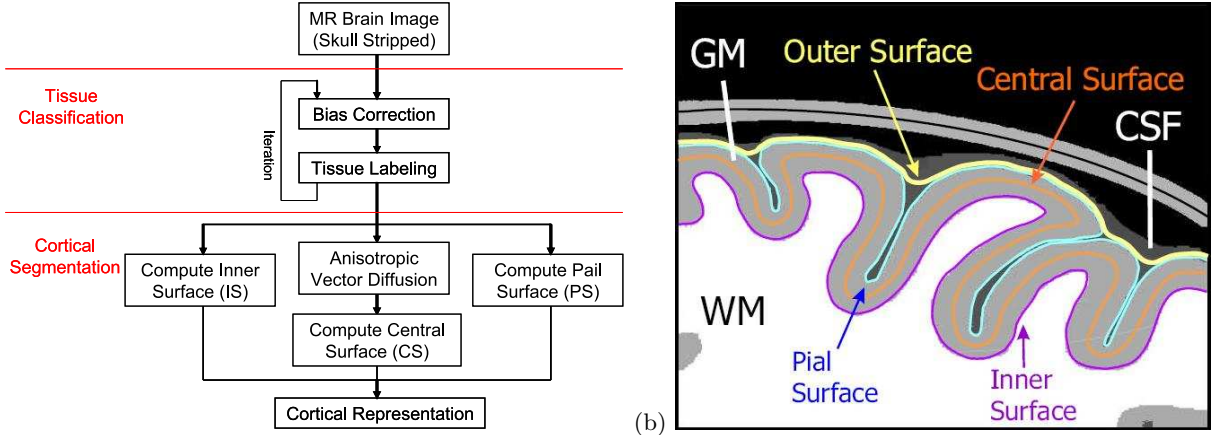


Figure 1. (a) Overview of our neuro image analysis pipeline. We aim to automatically extract important neuroanatomic structures depicted in (b). (b) (From [15, Figure 1.2].) A schematic drawing showing part of the cross section of a human brain and the definition of the cortical surfaces — *inner*, *central*, *pial*, and *outer* surfaces.¹⁶

Brain cortex is typically represented as a set of surfaces: an inner surface located at the boundary between gray matter and white matter, and an outer pial surface located at the boundary between gray matter and cerebrospinal fluid. An abstract central surface is sometimes used to provide a geometric representation of the cortex. This surface is located roughly half way between the inner surface and the outer surface. Commonly used algorithms for reconstructing these surfaces are deformable surface models.^{6–11} In order to maintain surface topology, the deformation allowed at each step is usually small. Therefore, it can take many hours for the algorithms to converge.

We propose an automatic approach combining tissue classification with intensity correction into an unified framework. Figure 1(a) illustrates our neuro image analysis pipeline. The MR brain cortex after proper skull stripping is classified and segmented according to tissue types into membership functions of the gray matter (GM), white matter (WM), and cerebrospinal fluid (CSF), detailed in § 2. We then explicitly extract the cortical boundary surfaces, namely, the *inner* and *pial* surfaces in between the WM-GM and GM-CSF, respectively, via iso-surface functions derived from the membership functions (§ 3).

To further characterize the morphology of the cortex, we propose a novel approach to compute the *central* surface (*CS*), which traces the peak values of the GM membership function, by a simple level-set extraction from the arithmetic combination of the membership functions, Eq.(1). The central surface can be further localized by applying a *gradient vector diffusion* technique,¹² which effectively preserves the accuracy and robustness. Our central surface computation is fast, effective, and free of topological issues. The result is comparable to many advanced methods such as using *distance transform*, *gray-scale thinning*, or *ridge tracing* (§ 4). In this formulation, since the central surface is computed as the zero-th levelset of a function, the algorithm is very fast and efficient.

This work serves a building block for to a variety of neuro analysis applications. We demonstrate a major contribution in cortical thickness measurement, an important application to study brain maturation and neuroanatomy.¹³ The cerebral cortex is an thin, folded sheet of GM bounded in between WM and CSF. Brain cortex thickness can be defined in several ways,¹⁴ and the challenge is in how to achieve an intuitive, yet computational efficient definition that enables reliable measurement of the depth variations of a curvy, sheet-like cortical *volume*. The problem gets more complicated when the boundary is fuzzy due to partial volume effect, considering how the tissue segmentation is performed. By leveraging the extracted *CS*, the cortical thickness can then be measured as the thickness between *CS* and the surfaces bordering WM and CSF. Our image analysis pipeline is simple, generic, accurate, fast, yet fully automatic. (§ 5).

2. SEGMENTATION WITH INTENSITY FIELD CORRECTION

MR tissue classification by soft segmentation with intensity correction is a well-known, evolving topic. Review articles by Vovk *et al*⁴ and Hou⁵ provide a general overview of the field. The MR non-uniformities arise due to

AFCM-RF Initialization:

1. Smooth the input MR image $y[j]$, where j is the index of individual pixels.
2. Detect non-background bounding box B. Divide B into $n \times n \times n$ grids $\{G_i | i = 1 \dots n^3\}$, e.g., $n=3, 4$, or 5 .
3. Initialize the gain field $g[j]$ of each voxel to 1.
4. Allocate space for the membership functions $\mu_1[j]$ for CSF, $\mu_2[j]$ for GM, $\mu_3[j]$ for WM.

AFCM-RF Iterations:

- A1. Run **FCM Classification** to obtain (μ_1, μ_2, μ_3) and intensity centroids (v_1, v_2, v_3) for each grid G_i .
- A2. Perform quadratic regression on the $n \times n \times n$ grids to estimate the gain field $g[j]$ of the whole image, by fitting the values of v_3 (WM) in all blocks.
- A3. Correct the intensity y by the updated gain field g : $y'[j] = y[j]/g[j]$.
- A4. Test convergence: If $y' - y$ are less than a threshold, exit.[†] Otherwise, repeat to Step A1.

FCM Classification — Initialization:

1. Initialize v_1, v_2, v_3 for each class by a histogram analysis on $y[j]$ in an image grid G_i .

FCM Classification — Iterations:**Repeat**

- F1. Compute new membership functions μ_1, μ_2, μ_3 by:

$$\mu_k[j] = \frac{(y[j] - v_k)^{-2}}{(y[j] - v_1)^{-2} + (y[j] - v_2)^{-2} + (y[j] - v_3)^{-2}}, \quad k = 1 \dots 3.$$

- F2. Compute new centroids v_1, v_2, v_3 of each class.

$$v_k = \frac{\sum_j (\mu_k[j])^2 \cdot y[j]}{\sum_j (\mu_k[j])^2}, \quad k = 1 \dots 3.$$

- F3. Compute new membership functions $(\mu_1^n, \mu_2^n, \mu_3^n)$ using Step F1 and test convergence with (μ_1, μ_2, μ_3) .

Until all membership values μ_k converges.

Table 1. Pseudo code of our AFCM-RF tissue classification and gain field correction algorithm. The FCM steps mimic the original approach summarized in.¹ [†]Footnote: To simplify the computation, we compare v_k of each class in all grids other than the whole image block. We test convergence based on the sum of square difference (SSD) of all v_k . The SSD tends to decrease as the intensity field g is compensated in the iterations. At some point when the SSD value increases, a convergence is reached.

phase differences in the radio-frequency field during acquisition. Many approaches has been proposed to correct such intensity inhomogeneity automatically. Wells *et al.*² described an expectation-maximization method that models the inhomogeneities as a gain field and iterate a classification step and a correction step in a supervised learning framework. Li *et al.*³ proposed a variational level-set approach for segmentation and gain field bias correction. Pham and Prince 's adaptive fuzzy segmentation approach¹ estimates the intensity centroids of each tissue class and the bias field in an iterative scheme, where the differential equation of the bias field and the soft segmentation are solved simultaneously using a multi-grid framework. This method enforces a smoothness constraint term in the energy minimization, which is computationally expensive.

Our approach follows the Adaptive Fuzzy C-Mean (AFCM) paradigm¹ with a different solution in correcting the inhomogeneous gain field using parametric *regression fitting*. We model the true underlying image with homogenous gain as the product of a *smooth* gain field (or bias field) g with the observed image. We estimate g and tissue labelling in an integrated process, which iterates on two main steps — a fuzzy clustering step for tissue labelling and a gain field estimating step for intensity correction. The iteration stops when both the gain field estimation and the tissue labelling have changes below a pre-defined threshold. The major difference in our approach to¹ is on how the gain field is estimated. Our novelty is the use of a simple regression method to estimate the bias field via parametric fitting. Our fuzzy clustering step mimics the original Fuzzy C-Mean (FCM) algorithm¹⁷ (summarized in¹), which in particular can be applied in any region of interest. We use a set of membership functions $\{\mu_k\}$ to characterize the likelihood of which each voxel belongs to a certain tissue class, where μ_k takes values between 0 and 1. If the intensity of a voxel is close to the prototypical centroid v_k of a class, its membership value is high (close to 1), indicating this voxel should belong to this class. The summation

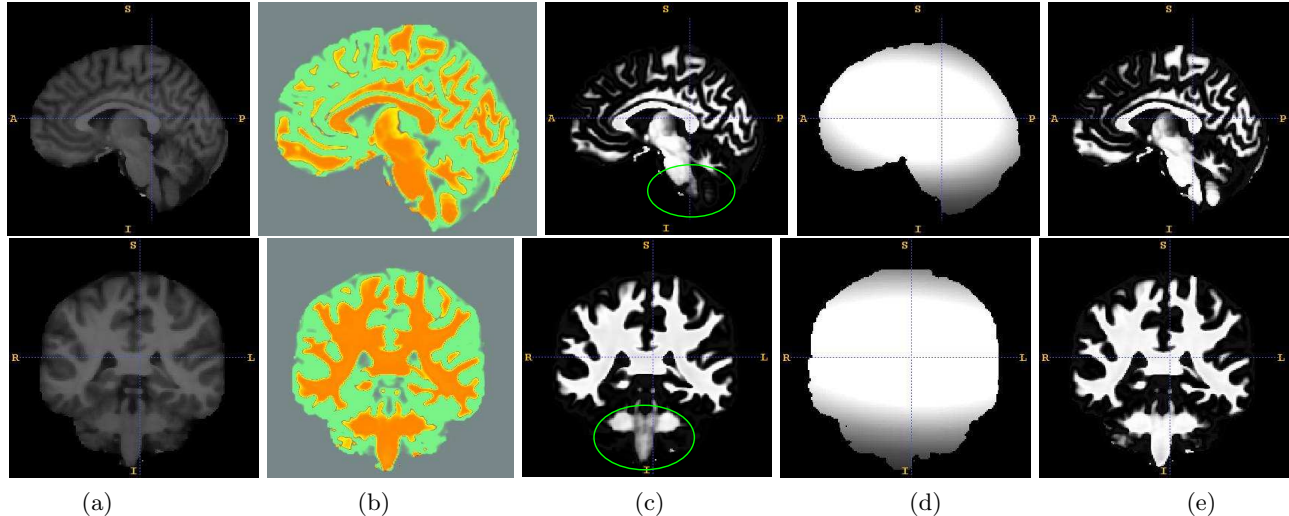


Figure 2. Result of the AFM-RF automatic tissue classification with gain field correction on a MR image from the OASIS dataset.²⁰ Upper: sagittal views. Bottom: coronal views. (a) Input MR image after initial smoothing. (b) Blending the segmented GM (green) and WM (orange) membership functions. (c) WM membership image extracted from FCM without bias correction. Observe that in the bottom part, the segmentation of the brainstem is incomplete and the cerebellum is missing due to low gain value. (d) Estimated gain field, where the lowest value at the bottom is 158 out of 255. The visualization is adjusted to emphasize image contrast. (e) WM membership image extracted from AFM-RF, where both the brainstem and cerebellum are correctly segmented.

of all classes of $\{\mu_k\}$ in each voxel is always 1.

Our tissue segmentation approach, the Adaptive Fuzzy C-Mean with Regression Fitting (AFM-RF) algorithm, is described as follows (see Table 1 for an overview). We implemented the original FCM fuzzy labelling technique as a component to integrate with our gain field correction framework. The FCM composes of an initialization and a propagation step. During initialization, we pre-smooth the input image using *gradient anisotropic smoothing* (Perona-Malik)¹⁸ and estimate the initial intensity centroids v_k^0 of each tissue class via a histogram analysis. Specifically, we iteratively select the mode of the histogram using a smoothed kernel estimator until the number of modes equal to the desired number of classes ($C=3$): class $i=1$ for CSF, $i=2$ for GM, and $i=3$ for WM. In the propagation step, the membership functions $\{\mu_k\}$ and the tissue centroids v_k are updated iteratively until the convergence of the gain field estimation is achieved.

The gain field estimation and correction in AFM-RF is based on two assumptions: (i) g is smooth; and (ii) the intensity variation depends only on location, but not on tissue classes. These assumptions enable us to model the g in a parametric form. In particular, we model g as a polynomial function in the 3D space (x, y, z) , which is solved via space division and parametric regression. We first divide the non-background image volume into n^3 blocks (*e.g.*, $n = 3, 4, \text{ or } 5$), assuming that each block contains sufficient components of tissues of all tissue classes. We then perform the above FCM tissue labelling within each block and obtain a set putative intensity centroids v_1, v_2, v_3 for tissue classes of CSF, GM, and WM, respectively. We use v_3 in the block grids to estimate the parameters of the gain field g by regression and fitting, since the WM has the strongest signal and is most reliable and pervasive. * We found that quadratic regression outperform the other types of regressions, such as linear, cubic, and higher orders. We continue to correct the image intensity using g and perform tissue labelling again in an iterative fashion, until the entire process converges.

Table 1 lists the pseudo code of our AFM-RF tissue classification algorithm. Our approach allows to mask any arbitrary region and perform segmentation and intensity correction only in that region, which is suitable to combine with other neuro analysis process, such as the skull stripping technique reported in.¹⁹ It is fully automatic. On average, it takes 3-5 minutes of computer time before convergence. Figure 2 shows an example result on a typical dataset from the OASIS database.²⁰

* Another option is to estimate g from the combination of $\{v_k\}$ from all classes.

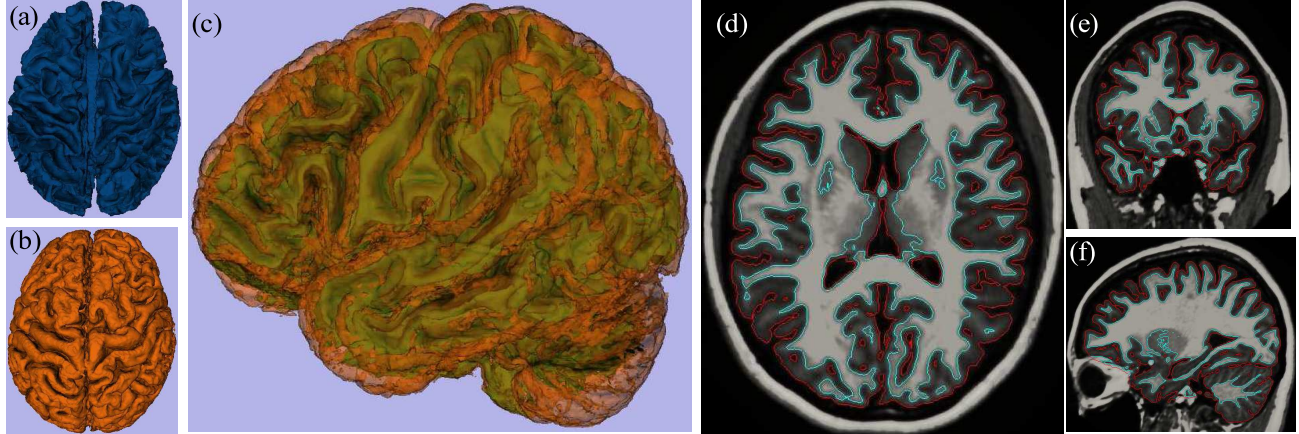


Figure 3. Segmentation of the cortex in a surface mesh form. The inner surface (\mathcal{IS}) in (a), pial surface (\mathcal{PS}) in (b), and the superimposition of them in a transparent view in (c). Observe how the GM cortex is delineated between these two surfaces. (d-f) Superimposing (a) and (b) onto the original MR image in the axial, coronal, and sagittal views.

3. EXTRACTING THE CORTEX BOUNDARY SURFACES

We extract the surfaces of cortical boundaries by using the labelled tissue membership functions $\mu_{csf} = \mu_1, \mu_{gm} = \mu_2, \mu_{wm} = \mu_3$. We denote the WM-GM boundary as the *inner* surface (\mathcal{IS}), and the GM-CSF boundary as the *pial* surface (\mathcal{PS}), respectively, as depicted in Figure 1(b).

The inner surface (\mathcal{IS}) is defined as the iso-surface where the WM and GM membership values are equal, $\mu_{wm} = \mu_{gm}$. \mathcal{IS} is extracted as the zero-th level-set of the level-set function $\phi_{\mathcal{IS}} = \mu_{wm} - \mu_{gm}$.

Similarly, the pial surface (\mathcal{PS}) is the set where $\mu_{gm} = \mu_{csf}$, which can be computed as the zero-th level-set of $\phi_{\mathcal{PS}} = \mu_{csf} - \mu_{gm}$. Since the CSF signal is generally weaker than the WM and GM signals (due to partial volume effect), in practice we use the fact that $\mu_{wm} + \mu_{gm} + \mu_{csf} = 1$ and re-define \mathcal{PS} as $\phi_{\mathcal{PS}}^1 = \mu_{wm} + \mu_{gm}$ with value 0.5. The iso-surface of this new definition yields a more reliable and visually pleasant result. Figure 3 shows an example of the extracted cortical surfaces \mathcal{IS} and \mathcal{PS} .

4. EXTRACTING THE CORTICAL CENTRAL SURFACE

We compute the “center” of the cortex by tracing the peak values (or *ridges*) of the GM membership function μ_{gm} to arrive at an abstract representation of the cortex. The collection of such GM ridge traces is in general a *surface* form, which we denote the *central* surface (\mathcal{CS}). Figure 5 illustrates an example of the \mathcal{CS} computed using the proposed method detailed below. Figure 4(a) shows the intersection of this \mathcal{CS} with a slice of μ_{gm} .

The computation of the peak values of GM grayscale map can be viewed as a *skeletonization* of the 3D grayscale image. In the literature there are several algorithms to perform such task, including (i) using *distance transform*^{21,22} for thinning, (ii) *grayscale thinning*²³ of 2D/3D images, (iii) *ridge tracing* on the 3D grayscale image,²⁴ and (iv) skeletonization using gradient vector diffusion.¹²

We compute the \mathcal{CS} using a simple but effective level-set approach, by using the pre-computed membership functions $\{\mu_k\}$ in the tissue labelling process described in § 2. The central surface is computed as the zero-th level-set of the following function:

$$\phi_{\mathcal{CS}}^0 = (\mu_{wm} - \mu_{csf}) \cdot (1 - \mu_{gm}). \quad (1)$$

The drawing in Figure 4(b) illustrates a schematic profile view of $\mu_{wm}, \mu_{gm}, \mu_{csf}$ along the cross-section of the cortical surface. Observe how the zero-th level value in the profile view of $(\mu_{wm} - \mu_{csf})$ motivates our level-set approach. The first term in Eq.(1) essentially separates the two sides of the GM ridge in different signs: the WM side approaches +1 and the CSF side approaches -1. The second term of Eq.(1) is used to constraint the GM peak to approach 0.

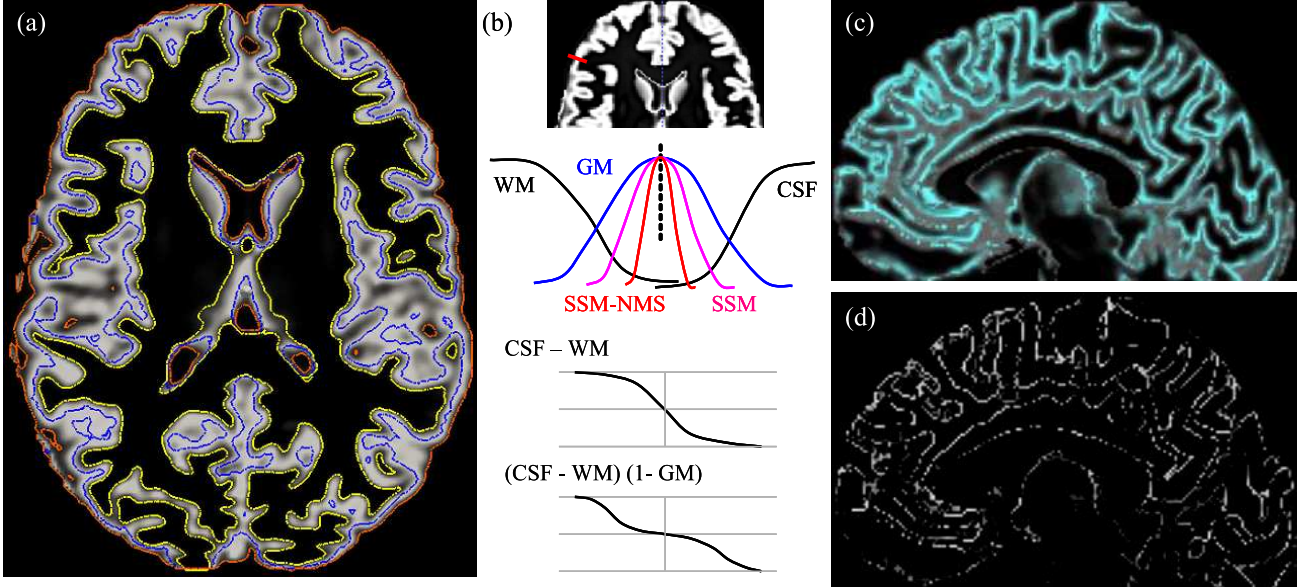


Figure 4. (a) An axial view of the IS (red), CS (blue), and PS (yellow) on top of the GM membership function μ_{gm} (in gray). (b) Upper: a cropped view of the GM membership function. Middle: Schematic illustration of the membership profile across the cortical surface (as marked in a red line in (b) Upper); see text for explanation. Bottom: Illustration for the derivation of Eq. (1). (c) The skeleton strength map μ_{ssm} (in blue) superimposed on top of μ_{gm} . (d) μ_{nms} , μ_{ssm} after non-maximum suppression. Observe how the peak of μ_{gm} is traced out by μ_{nms} , even there is heavy discretization in this 2D slice view.

Note that the intensity of the GM membership function μ_{gm} near the GM ridge is typically smooth and non-sharp (observe this in Figure 4(a,b)), which could degrade the accuracy in localizing the central surface CS using Eq. 1. In order to accurately localize CS , we apply the technique of *anisotropic gradient vector diffusion* (AGVD) on μ_{gm} to enhance its ridge structures. The AGVD was first proposed in¹² for 2D images, and here we extend it into 3D. Specifically, we extend the AGVD in 3D to compute a *skeleton strength map* (SSM),¹² denoted as μ_{ssm} , which after normalization enhances the peak of the GM. Figure 4(c) shows an example of μ_{ssm} in localizing the peak of μ_{gm} . We further enhance the peak by applying *non-maximum suppression*, where the result is denoted as μ_{nms} . Finally, based on these improvements, the central surface is extracted by using the zero-th level-set of the following function:

$$\phi_{CS} = (\mu_{wm} - \mu_{csf}) \cdot (1 - \mu_{gm}) \cdot (1 - \mu_{nms}). \quad (2)$$

To maintain a clear flow of exposition in our main approach, we omit the derivation of the isotropic and anisotropic gradient vector diffusion.^{12,25} Instead we describe the details in the Appendix, where we summarize the key derivations and main equations of AGVD in the 3D case for completeness.

5. MEASURING THE CORTICAL THICKNESS

Our representation of the cortex in the form of multiple surfaces (*i.e.*, the IS , CS , and PS) has lead to practical applications. As a demonstration, we describe a robust and accurate approach to measure cortical thickness.

The problem of measuring cortical thickness is challenging due to the highly convoluted nature of the cortex. In general, the thickness of this cortical volume in 3D is indeed difficult to define — an *orientation* must be formulated adaptively and consistently to measure the depth. Not to mention that the segmentation could be fuzzy and no explicit surface boundary is available.

In the literature the cortical thickness has been computed using several distinct approaches. Yezzi and Prince¹⁴ defined thickness as a smooth vector field describing the *length of correspondence trajectories* from one boundary to the other and solve it using an Eulerian PDE framework. Das *et al.*^{26,27} measured the thickness

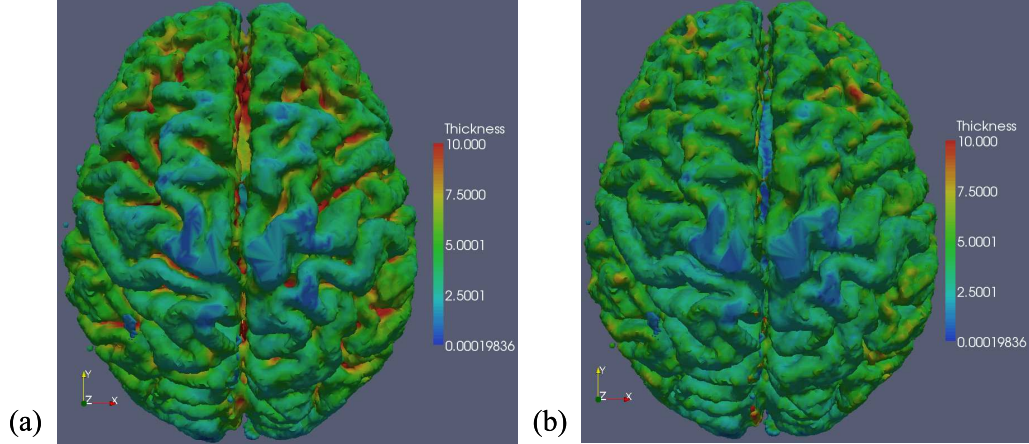


Figure 5. Visualization of cortical thickness measurements on the central surface (\mathcal{CS}) using d_{CT}^1 in (a) where the average thickness is 7.09 mm and d_{CT}^2 in (b) where the average thickness is 4.02 mm.

using a local surface model computed via a topology preserving segmentation. The GM thickness is defined as the distance between a WM surface point to the closest GM surface point along the WM surface normal direction \vec{n} . The GM thickness is then measured by integrating the GM probability map along the path of \vec{n} . This approach crucially depends on an accurate estimate of \vec{n} , which is obtained via fitting local surface model. A topology preserving segmentation is used to recover the GM in deep sulci. Hutton *et al.*²⁸ proposed a recent approach, where the thickness is modelled as a scalar field θ and formulated using a Laplace’s equation, which is solved at every voxel of the GM volume to calculate the normal direction to estimate thickness. In,²⁹ a similar voxel-based Laplacian definition of thickness is used. In this approach, subvoxel estimate of boundary is obtained through ray-casting using partial volume estimation and the direction of the streamlines. The boundary estimate is then used to initialize the boundary conditions to compute the streamline length.

Since we have computed the cortical surface boundaries (\mathcal{IS} and \mathcal{PS}) and the central surface \mathcal{CS} explicitly, we can intuitively define GM thickness according to criteria that suit application needs. For the purpose of illustration, we use two formulas to calculate cortical thickness from the surfaces. In the first one, the cortical thickness at any point \mathbf{x} on \mathcal{CS} is defined as the sum of distance of \mathbf{x} to \mathcal{IS} and the distance of \mathbf{x} to \mathcal{PS} , *i.e.*,

$$d_{CT}^1(\mathbf{x}) = d_{\mathcal{IS}}(\mathbf{x}) + d_{\mathcal{PS}}(\mathbf{x}). \quad (3)$$

This measurement is similar to the radius field defined by the *medial axis*. Secondly, due to the weaker CSF signal than the WM, a phenomena well-known in the literature²⁶ which often causes inaccuracy (unresolved sulci) and topological problems. We use twice of the GM-WM distance to measure cortical thickness, *i.e.*,

$$d_{CT}^2 = 2 \cdot d_{\mathcal{IS}}(\mathbf{x}). \quad (4)$$

The second thickness definition is more robust but its measurement quantity is relatively smaller than the first one. Figure 5 illustrates the results according to the two thickness measurements.

6. DISCUSSIONS AND CONCLUSION

We have proposed a unified framework to segment MR brain images using fuzzy classification with automatic bias field correction and gradient vector diffusion. The result is used to extract the cortical boundaries and the central surface to better model the cortex morphology. Our surface representation of the cortex contains less topological issues and does not require complex post-processing in comparing to other methods such as *ridge tracing*. It is free of topology constraints in comparing to the *deformable model* methods. We have demonstrated a practical application in measuring cortical thickness. Our framework is promising for further investigations.

Future works include validation of our algorithm and comparison with other published work at assess the performance. Careful investigation on topology properties of the resulting surfaces is also needed. We will explore the application areas of surface based analysis using the surface reconstructed from the proposed algorithm.

APPENDIX A. GRADIENT VECTOR DIFFUSION IN LOCALIZING THE CENTRAL SURFACE

The *gradient vector diffusion* (GVD) technique developed by Xu and Prince²⁵ is commonly used for applications such as the smoothing of a noisy vector field and to propagate non-zero vectors towards areas of zero vectors. The diffusion of a vector field, for example the gradient vector field, can be *isotropic* in resembling a distance transform or be *anisotropic*, depending on application needs. Yu and Bajaj¹² has exploited the use of GVD in the skeletonization of 2D grayscale images. In this appendix, we extend the use of GVD in the skeletonization of the 3D gray matter (GM) membership map, which leads to a better localization of the central surface. We describe the initialization of the gradient field in § A.1. We then derive the key equations to perform the isotropic diffusion of the vector field in § A.2 and the anisotropic diffusion in § A.3. The main result of this appendix are essentially the extension of the works in²⁵ and¹² to the 3D case.

A.1 Gradient Vector Initialization

For an input 3D scalar image $I(\vec{r}) = I_{[x,y,z]}$ taking intensity value between 0 and 1, we assume the foreground object has intensity brighter than the background. The gradient vector field is initialized as:¹²

$$gvf(\vec{r}) = \left(I(\vec{r}) - I(\vec{r}^j) \right) \times \frac{\vec{r}^j - \vec{r}}{\|\vec{r}^j - \vec{r}\|},$$

where $I(\vec{r}^j)$ is one of the $3 \times 3 \times 3$ neighboring pixels with lowest intensity. The first term defines the magnitude and second term defines the direction of each vector at each pixel location. This initial vector field resembles an edge detection result of I , which is a vector field encodes both the gradient intensity and its direction.

A.2 Isotropic Gradient Vector Diffusion

We denote the vector field in diffusion as $(u, v, w) = (u_{[x,y,z]}, v_{[x,y,z]}, w_{[x,y,z]})$, which is initialized using Eq.(A.1). The Laplacian operator is denoted as ∇^2 . The PDE for isotropic gradient vector diffusion is:

$$\begin{cases} \frac{du}{dt} = \eta \cdot \nabla^2 u = \frac{\partial^2 u}{\partial x^2} + \frac{\partial^2 u}{\partial y^2} + \frac{\partial^2 u}{\partial z^2} \\ \frac{dv}{dt} = \eta \cdot \nabla^2 v = \frac{\partial^2 v}{\partial x^2} + \frac{\partial^2 v}{\partial y^2} + \frac{\partial^2 v}{\partial z^2} \\ \frac{dw}{dt} = \eta \cdot \nabla^2 w = \frac{\partial^2 w}{\partial x^2} + \frac{\partial^2 w}{\partial y^2} + \frac{\partial^2 w}{\partial z^2}, \end{cases} \quad (5)$$

where η is a regularization parameter reflecting the noise level. We use $\eta = 100$. One can increase η to handle cases with stronger noise. The diffused vector field (u, v, w) in the above PDE can be solved using the following finite difference equation, which is essentially an implementation of the 2D discrete Laplacian operator $\begin{bmatrix} 1 & 1 & 1 \\ 1 & -4 & 1 \\ 1 & 1 & 1 \end{bmatrix}$ in the 3D case, where the central value -4 is now -6 :

$$\begin{cases} \frac{u_{[i,j,k]}^{n+1} - u_{[i,j,k]}^n}{\Delta t} = \frac{\eta}{\Delta x \Delta y} \cdot \left(u_{[i+1,j,k]}^n + u_{[i,j+1,k]}^n + u_{[i,j,k+1]}^n + u_{[i-1,j,k]}^n + u_{[i,j-1,k]}^n + u_{[i,j,k-1]}^n - 6u_{[i,j,k]}^n \right) \\ \frac{v_{[i,j,k]}^{n+1} - v_{[i,j,k]}^n}{\Delta t} = \frac{\eta}{\Delta x \Delta y} \cdot \left(v_{[i+1,j,k]}^n + v_{[i,j+1,k]}^n + v_{[i,j,k+1]}^n + v_{[i-1,j,k]}^n + v_{[i,j-1,k]}^n + v_{[i,j,k-1]}^n - 6v_{[i,j,k]}^n \right) \\ \frac{w_{[i,j,k]}^{n+1} - w_{[i,j,k]}^n}{\Delta t} = \frac{\eta}{\Delta x \Delta y} \cdot \left(w_{[i+1,j,k]}^n + w_{[i,j+1,k]}^n + w_{[i,j,k+1]}^n + w_{[i-1,j,k]}^n + w_{[i,j-1,k]}^n + w_{[i,j,k-1]}^n - 6w_{[i,j,k]}^n \right). \end{cases} \quad (6)$$

We set the grid size $\Delta x = \Delta y = 1$ in our case. Δt is a parameter related to the *stability* of the PDE. Let $\rho = \frac{\eta \Delta t}{\Delta x \Delta y}$. The finite difference equations is then:

$$\begin{cases} u_{[i,j,k]}^{n+1} = u_{[i,j,k]}^n + \rho \cdot \left(u_{[i+1,j,k]}^n + u_{[i,j+1,k]}^n + u_{[i,j,k+1]}^n + u_{[i-1,j,k]}^n + u_{[i,j-1,k]}^n + u_{[i,j,k-1]}^n - 6u_{[i,j,k]}^n \right) \\ v_{[i,j,k]}^{n+1} = v_{[i,j,k]}^n + \rho \cdot \left(v_{[i+1,j,k]}^n + v_{[i,j+1,k]}^n + v_{[i,j,k+1]}^n + v_{[i-1,j,k]}^n + v_{[i,j-1,k]}^n + v_{[i,j,k-1]}^n - 6v_{[i,j,k]}^n \right) \\ w_{[i,j,k]}^{n+1} = w_{[i,j,k]}^n + \rho \cdot \left(w_{[i+1,j,k]}^n + w_{[i,j+1,k]}^n + w_{[i,j,k+1]}^n + w_{[i-1,j,k]}^n + w_{[i,j-1,k]}^n + w_{[i,j,k-1]}^n - 6w_{[i,j,k]}^n \right). \end{cases} \quad (7)$$

The convergence condition is $\Delta t \leq \frac{\Delta x \Delta y}{6\eta}$. We found that 10 iterations of the above finite difference scheme are sufficient to produce a good diffusion vector field in (u, v, w) .

A.3 Anisotropic Gradient Vector Diffusion

Yu and Bajaj¹² have shown that the anisotropic gradient vector diffusion outperform the isotropic diffusion in producing a stronger skeleton strength map. We borrow the notation from¹² and derive the PDE for anisotropic gradient vector diffusion as:

$$\begin{cases} \frac{du}{dt} = \eta \cdot \text{div}(\alpha(\vec{c}, \vec{s}) \cdot \nabla u) \\ \frac{dv}{dt} = \eta \cdot \text{div}(\alpha(\vec{c}, \vec{s}) \cdot \nabla v) \\ \frac{dw}{dt} = \eta \cdot \text{div}(\alpha(\vec{c}, \vec{s}) \cdot \nabla w), \end{cases} \quad (8)$$

where div denotes the *divergence* of a vector field. The anisotropic diffusion function α is a decreasing function reflecting the amount of anisotropic diffusion, which depends on the angle θ between the central vector \vec{c} of a pixel location and one of its surrounding vector \vec{s} in the $3 \times 3 \times 3$ neighborhood. We want α to approach 0 as the angle between (\vec{c}, \vec{s}) approaches π , to slow down the diffusion when vectors are in opposite directions. Similarly, we want α to increase as the angle between (\vec{c}, \vec{s}) approaches 0, such that the diffusion speeds up when neighboring vectors align well. We use the following definition of α as an extension of¹² to 3D:

$$\alpha(\theta) = \alpha(\vec{c}, \vec{s}) = \begin{cases} e^{2\left(\frac{\vec{c} \cdot \vec{s}}{\|\vec{c}\| \|\vec{s}\|} - 1\right)} & \text{if } \vec{c} \neq 0 \text{ and } \vec{s} \neq 0 \\ 0 & \text{if } \vec{c} = 0 \text{ or } \vec{s} = 0. \end{cases} \quad (9)$$

We compute the anisotropic gradient vector diffusion as follows:

1. Compute the anisotropic gradients of the three components of (u, v, w) : $\nabla u = (u_{dx}, u_{dy}, u_{dz})$, $\nabla v = (v_{dx}, v_{dy}, v_{dz})$, and $\nabla w = (w_{dx}, w_{dy}, w_{dz})$ at each pixel.
2. Compute the anisotropic diffusion function of the three components: $\alpha_u(\theta)$, $\alpha_v(\theta)$, $\alpha_w(\theta)$.
3. Compute $\alpha^u = \alpha_u(\theta) \cdot \nabla u$, $\alpha^v = \alpha_v(\theta) \cdot \nabla v$, $\alpha^w = \alpha_w(\theta) \nabla w$. Denote the three components of α^u as $(\alpha_x^u, \alpha_y^u, \alpha_z^u)$; similarly, $\alpha^v = (\alpha_x^v, \alpha_y^v, \alpha_z^v)$, $\alpha^w = (\alpha_x^w, \alpha_y^w, \alpha_z^w)$.
4. Compute the divergence $\text{div}(\alpha^u)$, $\text{div}(\alpha^v)$, $\text{div}(\alpha^w)$ by considering the 6 neighbors in a $3 \times 3 \times 3$ block.

$$\begin{cases} \text{div}(\alpha^u)_{[i,j,k]} = \frac{\alpha_x^u_{[i+1,j,k]} - \alpha_x^u_{[i-1,j,k]}}{2\Delta x} + \frac{\alpha_y^u_{[i,j+1,k]} - \alpha_y^u_{[i,j-1,k]}}{2\Delta y} + \frac{\alpha_z^u_{[i,j,k+1]} - \alpha_z^u_{[i,j,k-1]}}{2\Delta z} \\ \text{div}(\alpha^v)_{[i,j,k]} = \frac{\alpha_x^v_{[i+1,j,k]} - \alpha_x^v_{[i-1,j,k]}}{2\Delta x} + \frac{\alpha_y^v_{[i,j+1,k]} - \alpha_y^v_{[i,j-1,k]}}{2\Delta y} + \frac{\alpha_z^v_{[i,j,k+1]} - \alpha_z^v_{[i,j,k-1]}}{2\Delta z} \\ \text{div}(\alpha^w)_{[i,j,k]} = \frac{\alpha_x^w_{[i+1,j,k]} - \alpha_x^w_{[i-1,j,k]}}{2\Delta x} + \frac{\alpha_y^w_{[i,j+1,k]} - \alpha_y^w_{[i,j-1,k]}}{2\Delta y} + \frac{\alpha_z^w_{[i,j,k+1]} - \alpha_z^w_{[i,j,k-1]}}{2\Delta z}. \end{cases} \quad (10)$$

5. The finite difference equation to solve the anisotropic diffusion PDE in Eq.(8) is :

$$\begin{cases} u_{[i,j,k]}^{n+1} = u_{[i,j,k]}^n + \eta \Delta t \cdot \text{div}(\alpha^u)_{[i,j,k]} \\ v_{[i,j,k]}^{n+1} = v_{[i,j,k]}^n + \eta \Delta t \cdot \text{div}(\alpha^v)_{[i,j,k]} \\ w_{[i,j,k]}^{n+1} = w_{[i,j,k]}^n + \eta \Delta t \cdot \text{div}(\alpha^w)_{[i,j,k]}. \end{cases} \quad (11)$$

Figure 6 shows an example result of the anisotropic gradient vector diffusion in localizing the central surface of the GM.

REFERENCES

- [1] Pham, D. L. and Prince, J. L., "Adaptive fuzzy segmentation of magnetic resonance images," *IEEE Trans. on Medical Imaging* **18**(9), 737–752 (1999).
- [2] Wells, W. M., Grimson, W. E. L., Kikinis, R., and Jolesz, F. A., "Adaptive segmentation of MRI data," *IEEE Trans. on Medical Imaging* **15** (August 1996).

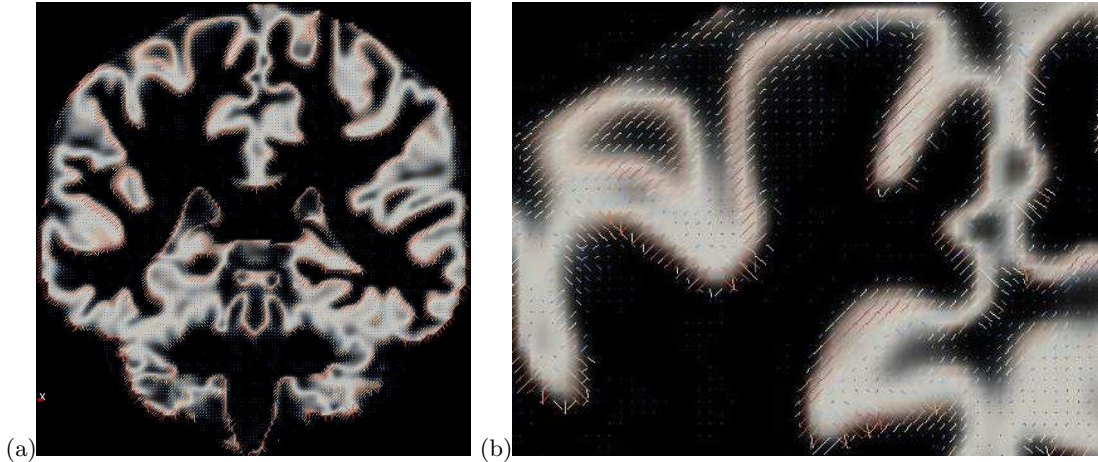


Figure 6. The gradient vector field on top of a coronal slice of μ_{gm} after a few iterations of anisotropic diffusion. (b) zooms in to the upper-left of (a). Vectors occluded by the μ_{gm} slice is not shown. Red and blue depict vectors in opposite directions. This 3D diffused vector field has opposite directions at the ridge of μ_{gm} , which also coincide with the trace of the CS.

- [3] Li, C., Huang, R., Ding, Z., Gatenby, C., Dimitris, M., and Gore, J., “A variational level set approach to segmentation and bias correction of images with intensity inhomogeneity,” in *[Proceedings of the 11th International Conference on Medical Image Computing and Computer-Assisted Intervention (MICCAI), Part II]*, 1083–1091, Springer-Verlag (2008).
- [4] Vovk, U., Pernus, F., and Likar, B., “A review of methods for correction of intensity inhomogeneity in MRI,” *IEEE Trans. Med. Imag.* **26**, 405–421 (March 2007).
- [5] Hou, Z., “A review on MR image intensity inhomogeneity correction,” *Int. J. Biomed. Imag.* **2006**, 1–11 (2006).
- [6] Xu, C., Pham, D., Rettmann, M., Yu, D., and Prince, J., “Reconstruction of the human cerebral cortex from magnetic resonance images,” *IEEE Transactions on Medical Imaging* **18**(6), 467–480 (1999).
- [7] Zeng, X., Staib, L., Schultz, R., and Duncan, J., “Segmentation and measurement of the cortex from 3D MR images,” *Lecture Notes in Computer Science*, 519–530 (1998).
- [8] Dale, A., Fischl, B., and Sereno, M., “Cortical surface-based analysis I. Segmentation and surface reconstruction,” *Neuroimage* **9**(2), 179–194 (1999).
- [9] Han, X., Pham, D., Tosun, D., Rettmann, M., Xu, C., and Prince, J., “CRUISE: cortical reconstruction using implicit surface evolution,” *NeuroImage* **23**(3), 997–1012 (2004).
- [10] MacDonald, D., Kabani, N., Avis, D., and Evans, A., “Automated 3-D extraction of inner and outer surfaces of cerebral cortex from MRI,” *NeuroImage* **12**(3), 340–356 (2000).
- [11] Goldenberg, R., Kimmel, R., Rivlin, E., and Rudzsky, M., “Cortex segmentation: A fast variational geometric approach,” *IEEE Transactions on Medical Imaging* **21**(12), 1544–1551 (2002).
- [12] Yu, Z. and Bajaj, C., “A segmentation-free approach for skeletonization of gray-scale images via anisotropic vector diffusion,” in *[IEEE Computer Society Conference on Computer Vision and Pattern Recognition (CVPR)]*, **1**, 415–420 (2004).
- [13] Scott, M. L. J., Bromiley, P. A., Thacker, N. A., and C. E. Hutchinson, A. J., “A fast, model-independent method for cerebral cortical thickness estimation using MRI,” *Medical Image Analysis* **13**, 269–285 (April 2009).
- [14] Yezzi, A. J. and Prince, J. L., “An Eulerian PDE approach for computing tissue thickness,” *IEEE Trans. on Medical Imaging* **22**, 1332–1339 (Oct. 2003).
- [15] Tao, X., *Statistical Geodesics and Shape Models: Finding Features for Registering Human Cortical Surfaces*, PhD thesis, Department of Electrical and Computer Engineering, Johns Hopkins University, Baltimore, Maryland (Jan. 2005).

- [16] Tosun, D., Rettmann, M. E., Naiman, D. Q., Resnick, S. M., Kraut, M. A., and Prince, J. L., “Cortical reconstruction using implicit surface evolution: Accuracy and precision analysis,” *NeuroImage* **29** (Feb. 2006).
- [17] Bezdek, J. C., “A convergence theorem for the fuzzy ISODATA clustering algorithms,” *IEEE Trans. Pattern Analysis and Machine Intelligence (PAMI)* **2**(1), 1–8 (1980).
- [18] Perona, P. and Malik, J., “Scale space and edge detection using anisotropic diffusion,” *IEEE Trans. on Pattern Analysis and Machine Intelligence* **12**(7), 629–639 (1990).
- [19] Tao, X. and Chang, M.-C., “A skull stripping method using deformable surface and tissue classification,” in [*SPIE Medical Imaging (Image Processing, Proceedings of SPIE Volume 7623*], to appear (2010).
- [20] Marcus, D. S., Wang, T. H., Parker, J., Csernansky, J. G., Morris, J. C., and Buckner, R. L., “Open access series of imaging studies (oasis): Cross-sectional MRI data in young, middle aged, nondemented, and demented older adults,” *Journal of Cognitive Neuroscience* **19**(9), 1498–1507.
- [21] Jang, J.-H. and Hong, K.-S., “A pseudo-distance map for the segmentation-free skeletonization of gray-scale images,” in [*ICCV*], **II**, 18–23 (2001).
- [22] Nedzved, A., Ablameyko, S., and Uchida, S., “Gray-scale thinning by using a pseudo-distance map,” in [*ICPR*], 239–242, IEEE Computer Society (2006).
- [23] Kim, K. M., Lee, B., Choi, N. S., Kang, G. H., Park, J. J., and Suen, C. Y., “Gray-scale thinning algorithm using local min/max operations,” *Document Analysis Systems VII, Lecture Notes in Computer Science* **3872**, 62–70 (2006).
- [24] Hirano, Y., Shimizu, A., ichi Hasegawa, J., and ichiro Toriwaki, J., “A tracking algorithm for extracting ridge lines in three-dimensional gray images using curvature of four-dimensional hypersurface,” *Systems and Computers in Japan* **32**(12), 25–37 (2001).
- [25] Xu, C. and Prince, J. L., “Snakes, shapes, and gradient vector flow,” *IEEE Trans. Image Processing* **7**, 359–369 (Mar. 1998).
- [26] Das, S. R., Avants, B. B., Grossman, M., and Gee, J. C., “Measuring cortical thickness using an image domain local surface model and topology preserving segmentation,” in [*Proc. IEEE International Conference on Computer Vision*], 1–8 (2007).
- [27] Das, S. R., Avants, B. B., Grossman, M., and Gee, J. C., “Registration based cortical thickness measurement,” *NeuroImage* **45**, 867–879 (Apr 2008).
- [28] Hutton, C., Vita, E. D., Ashburner, J., Deichmann, R., and Turner, R., “Voxel-based cortical thickness measurements in MRI,” *NeuroImage* **40**, 1701–1710 (May 2008).
- [29] Bourgeat, P., Zuluaga, O. A. M., Fripp, J., Salvado, O., and Ourselin, S., “Improved cortical thickness measurement from MR images using partial volume estimation,” in [*Biomedical Imaging: From Nano to Macro, ISBI*], 205–208 (2008).